Radioactive ^{198}Au-Doped Nanostructures with Different Shapes for *In Vivo* Analyses of Their Biodistribution, Tumor Uptake, and Intratumoral Distribution

Kvar C. L. Black,[†,∥] Yucai Wang,[‡,∥] Hannah P. Luehmann,[†] Xin Cai,[§] Wenxin Xing,[§] Bo Pang,[‡] Yongfeng Zhao,[†] Cathy S. Cutler,[⊥] Lihong V. Wang,[§] Yongjian Liu,[†,*] and Younan Xia[‡,*]

[†]Mallinckrodt Institute of Radiology, Washington University School of Medicine, St. Louis, Missouri 63110, United States, [‡]The Wallace H. Coulter Department of Biomedical Engineering, Georgia Institute of Technology and Emory University, Atlanta, Georgia 30332, United States, [§]Department of Biomedical Engineering, Washington University, St. Louis, Missouri 63130, United States, and [⊥]University of Missouri Research Reactor, Columbia, Missouri 65211, United States. [∥]These authors contributed equally to this work.

ABSTRACT With Au nanocages as an example, we recently demonstrated that radioactive ^{198}Au could be incorporated into the crystal lattice of Au nanostructures for simple and reliable quantification of their *in vivo* biodistribution by measuring the γ radiation from ^{198}Au decay and for optical imaging by detecting the Cerenkov radiation. Here we extend the capability of this strategy to synthesize radioactive ^{198}Au nanostructures with a similar size but different shapes and then compare their biodistribution, tumor uptake, and intratumoral distribution using a murine EMT6 breast cancer model. Specifically, we investigated Au nanospheres, nanodisks, nanorods, and cubic nanocages. After PEGylation, an aqueous suspension of the radioactive Au nanostructures was injected into a tumor-bearing mouse intravenously, and their biodistribution was measured from the γ radiation while their tumor uptake was directly imaged using the Cerenkov radiation. Significantly higher tumor uptake was observed for the Au nanospheres and nanodisks relative to the Au nanorods and nanocages at 24 h postinjection. Furthermore, autoradiographic imaging was performed on thin slices of the tumor after excision to resolve the intratumoral distributions of the nanostructures. While both the Au nanospheres and nanodisks were only observed on the surfaces of the tumors, the Au nanorods and nanocages were distributed throughout the tumors.

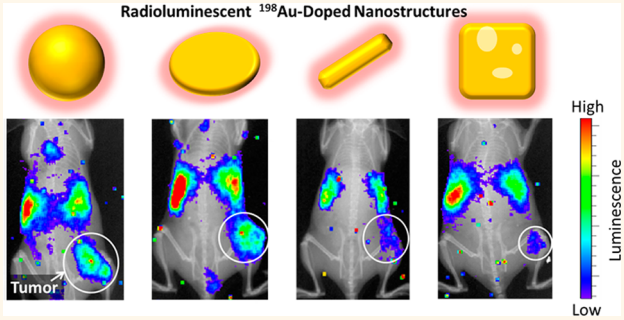

KEYWORDS: Cerenkov imaging · radioactive gold nanostructures · biodistribution · tumor uptake · intratumoral distribution · shape dependence

Nanostructures are of great importance for a wide variety of applications in cancer theranostics including imaging, drug delivery, and therapy.[1] Among various types of nanostructures, those based on Au have received increasing attention in recent years owing to their tunable localized surface plasmon resonance (LSPR) properties. Arising from the collective oscillation of conduction electrons confined to a nanoscale structure, the LSPR causes strong absorption and scattering of light at tunable wavelengths for optical imaging and photothermal destruction of tumors.[2−4] By forming anisotropic shapes such as nanorods, nanodisks, and nanocages, the LSPR can be tuned into the transparent window (700−900 nm) of soft tissues in the near-infrared (NIR) region to meet the requirements for *in vivo* application.[5] In addition, Au nanostructures can be functionalized with radioactive species for positron emission tomography (PET) imaging,[6] Cerenkov imaging,[7−9] and/or radiotherapy[10] through radiolabeling with β^+-emitting ^{64}Cu nuclides[6] or incorporation of β^--emitting

* Address correspondence to younan.xia@bme.gatech.edu, liuyo@mir.wustl.edu.

Received for review December 5, 2013 and accepted April 25, 2014.

Published online April 25, 2014
10.1021/nn406258m

^{198}Au isotopes.[11] Importantly, these radioactive imaging modalities, whether based on γ-rays or visible light, can be used not only for the *in vivo* biodistribution analysis of Au nanostructures but also for monitoring their uptake by the targeted disease site.

To fully realize their potential in cancer theranostics, the nanostructures must be able to enter the tumor and be evenly distributed throughout the tumor, which is composed of heterogeneous microenvironments containing both vascular and avascular volumes.[12] It has been established that nanostructures can enter a tumor by leaking out through the gaps between endothelial cells of the chaotic and hyperpermeable vasculature of a tumor through a mechanism known as the enhanced permeability and retention (EPR) effect.[13−16] The efficacy of this process depends on the physicochemical characteristics of the nanostructures, including both size and shape. It has been shown that spherical particles of 50−100 nm in diameter tend to present an optimal range of size for maximizing tumor accumulation due to the EPR effect and minimizing the subsequent clearance.[17−19] Compared to nanospheres, nanostructures with other shapes (*e.g.*, nanorods) can have distinct EPR effects due to alterations to their *in vivo* hydrodynamic behaviors such as circulation, transport in blood flow, and extravasation into the tumor.[20−25] However, due to the difficulty in generating nanostructures with the same uniform size but different shapes from the same material, the effect of shape on the EPR effect and thus tumor uptake still needs further assessment. In addition, the influence of size or shape of nanostructures on their *in vivo* intratumoral distribution is yet to be explored despite its paramount importance in cancer diagnosis and therapy. While it has been observed that rod-shaped nanostructures like carbon nanotubes tended to penetrate into the core of a tumor more effectively compared to their spherical counterparts like quantum dots,[26,27] there is essentially no study on the intratumoral distribution of nanostructures with similar sizes but different shapes, particularly those composed of Au with interesting LSPR properties.

Due to the great potential of Au nanostructures for oncological imaging and therapy, it is of great importance to systematically evaluate the effects of their shapes on biodistribution, tumor uptake, and intratumoral distribution. In this work, we accomplished these goals in a murine EMT6 breast cancer model by incorporating radioactive ^{198}Au (β^- = 0.96 MeV, $t_{1/2}$ = 2.7 days) into Au nanostructures with a similar size but four different shapes, including nanospheres, nanodisks, nanorods, and cubic nanocages. The radioactive ^{198}Au was directly incorporated into their crystal lattices during the syntheses with precisely controlled specific radioactivity. The characteristic γ emission from ^{198}Au was directly employed for a quantitative analysis of the biodistribution in a tumor-bearing mouse, whereas the Cerenkov luminescence derived from the β^- emission was used for monitoring tumor uptake *in vivo* and autoradiography imaging of intratumoral distribution *ex vivo*. We also performed photoacoustic (PA) imaging, PET imaging, and hematoxylin and eosin (H&E) histological staining to characterize tumor vascularity, hypoxia, metabolism, and spatial heterogeneity, respectively. Combined together, it can be concluded that incorporation of ^{198}Au into Au nanostructures offers a new platform to stably label nanostructures for quantitative measurements of biodistribution, tumor uptake, and intratumoral distribution. The data collected from such multimodal imaging demonstrated that the shape of Au nanostructures indeed played a critical role in determining their biodistribution, tumor uptake, and intratumoral distribution in a murine EMT6 breast cancer model, which can be further extended to other preclinical cancer models.

RESULTS AND DISCUSSION

Synthesis and Characterization of ^{198}Au-Incorporated Au Nanostructures. In this study, we employed the strategy of directly incorporating the radionuclide ^{198}Au into the crystal lattice of nanostructures to compare the tumor passive targeting efficiency and intratumoral distribution of Au nanostructures with four different shapes. As we recently demonstrated with Au nanocages,[11] the γ radiation from ^{198}Au could be used for quantitative analyses of biodistribution and tumor targeting efficacy, whereas the visible light generated from β^- emission could be employed for *in vivo* Cerenkov imaging. Here we further extended this approach to other types of Au nanostructures including nanospheres, nanodisks, and nanorods and then used these nanostructures as probes to understand the impacts of shape on their biodistribution, tumor targeting capability, and intratumoral distribution. Since the radionuclide is incorporated into the crystal lattice of a nanostructure, rather than attached to the surface through a molecular linker, we could accurately analyze the nanostructures *in vivo* without worrying about potential issues associated with the linker, including *in vivo* instability and changes to surface characteristics that will affect the biodistribution of nanostructures.[6]

The Au nanostructures were synthesized with a similar size (the largest dimension for those with a nonspherical shape) around 50 nm, which is known to display a significant EPR effect for tumor targeting (Supporting Information Table S1).[17] Four distinct shapes, including spherical,[28] disk-like,[29] rod-shaped,[30] and cubic,[6,31] were evaluated. Figure 1 shows TEM images of these nanostructures in the nonradioactive form. Figure S1 shows the LSPR spectra taken from their aqueous suspensions. The nanospheres had an LSPR peak at 532 nm, while the other three types of nanostructures all showed LSPR peaks in the NIR region

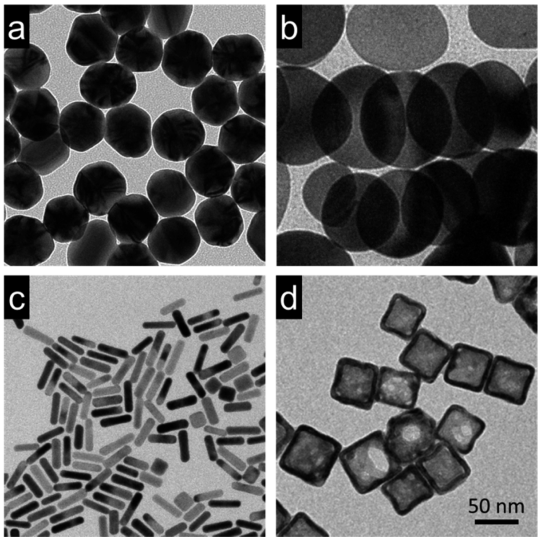

Figure 1. TEM images of the four different types of Au nanostructures in the nonradioactive version: (a) nanospheres, (b) nanodisks, (c) nanorods, and (d) cubic nanocages. The scale bar applies to all images.

due to their anisotropy in structure, rendering them potential *in vivo* theranostic agents. Specifically, the LSPR peaks of the nanodisks, nanorods, and nanocages were located at 769, 817, and 778 nm, respectively. To use the radioactive property for biodistribution analysis, luminescence imaging, and tumor autoradiographic imaging, ^{198}Au was directly incorporated into the crystal lattice of the Au nanostructure simply by mixing radioactive $H^{198}AuCl_4$ with nonradioactive $HAuCl_4$ prior to their use as the reagents for chemical reduction or galvanic replacement. For each sample of Au nanostructures, the specific radioactivity could be tightly controlled by varying the ratio of $H^{198}AuCl_4$ to $HAuCl_4$ in the mixture while keeping their total amount and therefore the LSPR properties of the resultant nanostructures unchanged.

Biodistribution of PEGylated, ^{198}Au-Incorporated Au Nanostructures. Once the ^{198}Au-incorporated Au nanostructures with four distinct shapes had been prepared and surface-functionalized with poly(ethylene glycol) (PEG, $M_W \approx 5000$), they were injected intravenously *via* the tail vein into mice bearing EMT6 tumors for a quantitative analysis of biodistribution by tracing the γ radiation from ^{198}Au. Since the ^{198}Au was incorporated into the lattice of each nanostructure, the ^{198}Au radiolabel showed good stability in mouse serum up to a week as we have demonstrated in a previous study.[11] By tracking the radiation emitted by ^{198}Au, we could accurately resolve the spatial distribution of the ^{198}Au-incorporated nanostructures. Similar to the biodistribution profiles previously reported for Au nanostructures,[3,6,32,33] all the samples of Au nanostructures showed high hepatic and splenic accumulation (Figures 2 and S2). However, for the Au nanostructures with different shapes, they displayed significant differences for the *in vivo* pharmacokinetic profiles. Specifically, the PEGylated Au nanospheres circulated in the bloodstream significantly longer than the other three types of nanostructures, with 24.8% injected dose per gram of tissue or blood (% ID/g) circulating at 6 h and 10.4% ID/g remaining in the blood at 24 h postinjection. The nanodisks showed moderate blood circulation, with 16.5% ID/g remaining in the blood at 1 h postinjection, 9.7% ID/g remaining after 6 h, and 0.5% ID/g after 24 h. The nanorods had the worst blood circulation compared with both nanospheres and nanodisks: 11.2% ID/g remained in the blood after 1 h, which further decreased to 0.9% ID/g at 6 h postinjection. The poor performance of Au nanorods can likely be attributed to the low coverage density of PEG chains on the surface due to slow replacement of the cetyltrimethylammonium bromide (CTAB) bilayer by PEG. Compared with the nanorods, the nanocages showed much better blood circulation, which hardly changed during the first 6 h (15.3 and 14.2% ID/g at 1 and 6 h, respectively). Although all types of Au nanostructures showed significant accumulation (20.7 to 43.9% ID/g, depending on the shape) in the liver at 1 h postinjection, the nanospheres showed the least clearance by the mononuclear phagocytic system (MPS), in particular, Kupffer cells in the liver. At 24 h, 34.9% ID/g of nanospheres was located in the liver compared to 55.0, 52.1, and 63.4% ID/g for the nanodisks, nanorods, and nanocages, respectively. Furthermore, a smaller portion of the nanospheres accumulated in the spleen relative to other samples, with 5.0% ID/g present at 24 h postinjection, compared to >40% ID/g for nanostructures with the other three shapes within the same time frame. Additional studies were also performed at 24 h postinjection to determine the clearance of these nanostructures by analyzing the Au contents in urine and feces through the use of inductively coupled plasma mass spectrometry. We did not observe any significant clearance for the four types of Au nanostructures used in the present work.

Due to their high blood retention and low clearance by the liver and spleen, the PEGylated Au nanospheres showed better accumulation in tumors than the nanostructures with other shapes, increasing from 2.1% ID/g at 1 h to 11.5% ID/g at 6 h and up to 23.2% ID/g at 24 h. The accumulation of nanodisks in tumors was observed to surge up to 6 h, increasing from 1.5% ID/g at 1 h to 4.4% ID/g at 6 h. Interestingly, the nanodisks remained in the lung more severely than any other shape, with 4.9% ID/g remaining at 24 h postinjection, suggesting other potential applications for pulmonary imaging or therapy. Due to the low blood circulation, the nanorods did not efficiently accumulate in the tumors, with less than 2.0% ID/g accumulated even at 24 h postinjection. The nanocages accumulated in tumors throughout the 24 h period, increasing from 1.2% ID/g at 1 h to 4.7% ID/g at 6 h and finally 7.5% ID/g at 24 h postinjection.

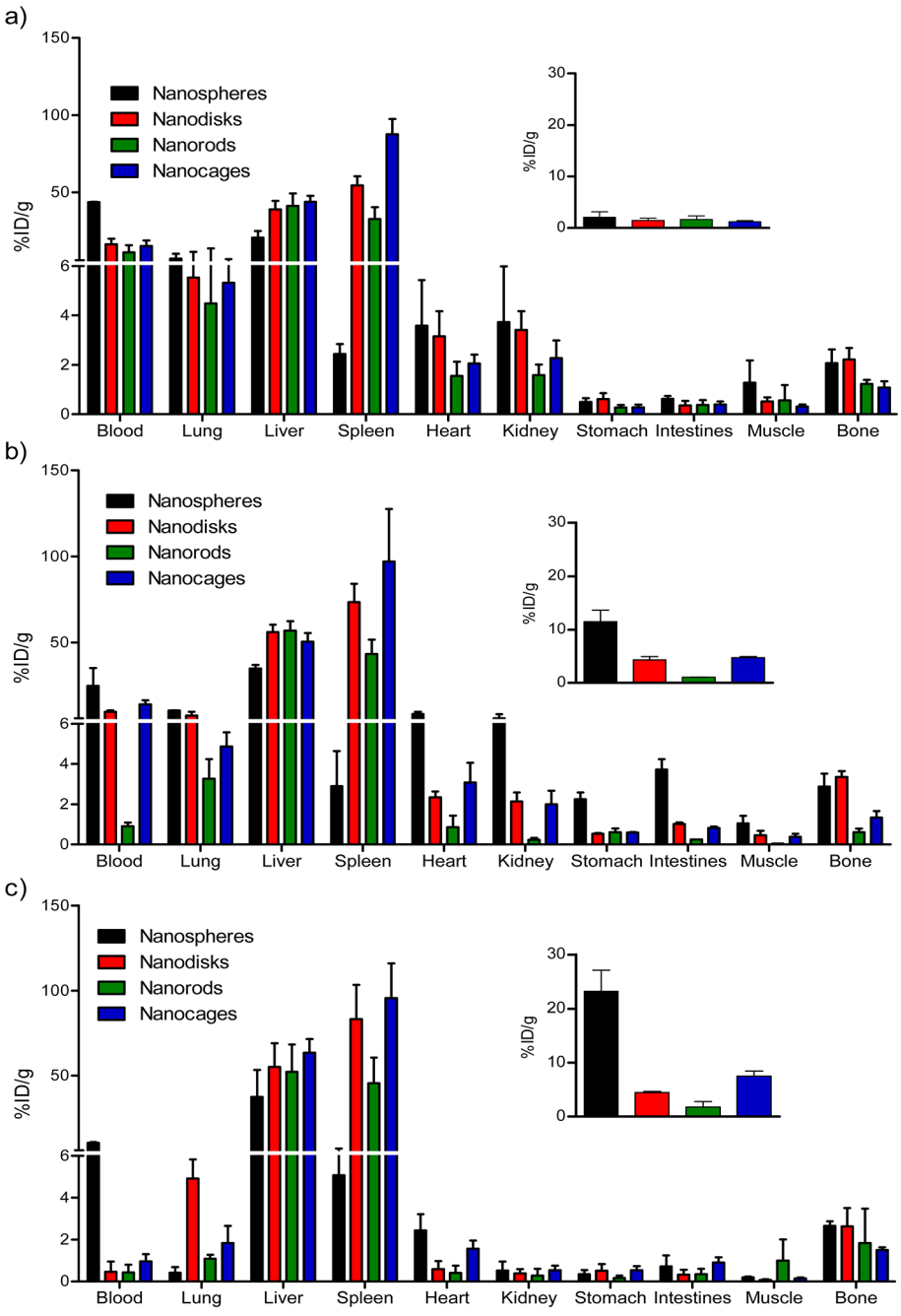

Figure 2. Biodistribution of the different types of ^{198}Au-incorporated Au nanostructures at (a) 1 h, (b) 6 h, and (c) 24 h postinjection, together with the tumor uptake data (insets). See Figure S2 for the biodistribution data in terms of % ID/organ.

***In Vivo* Luminescence Imaging.** In addition to quantitative analysis of biodistribution by following the γ emission, *in vivo* luminescence imaging was also performed on the mice bearing EMT6 tumors by monitoring the Cerenkov radiation with a conventional optical *in vivo* imaging system (IVIS).[11] Significantly, luminescence in the visible region could be detected with a low background from all the Au nanostructures *in vivo*, which could be used to resolve their locations through co-registration with the anatomical X-ray images. As illustrated in Figure 3, all the ^{198}Au-incorporated nanostructures showed accumulation in the tumors in the optical images captured at 24 h postinjection. The luminescence intensities from tumors in mice injected with the nanospheres, nanodisks, and nanocages increased throughout the 24 h period. The changes in luminescence intensity over time generally matched the kinetic data obtained for all the four samples (Figure S3). These data are in agreement with the time-dependent biodistribution shown in Figure 2. In addition, luminescence was observed in areas corresponding to liver and spleen after the injection of all the Au nanostructures. Much stronger luminescence was recorded from the tumor region for both the

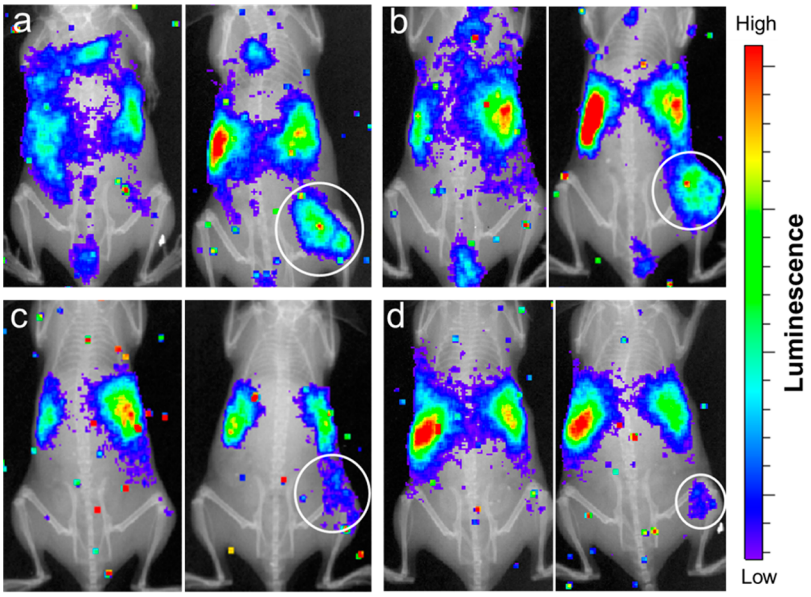

Figure 3. Co-registered *in vivo* luminescence and X-ray images of the tumor-bearing mice at 1 h (left panel) and 24 h (right panel) postinjection of the different types of ^{198}Au-incorporated nanostructures: (a) nanospheres, (b) nanodisks, (c) nanorods, and (d) cubic nanocages.

nanospheres (Figure 3a, 4.7 $\times$ 10^4 counts) and nanodisks (Figure 3b, 3.9 $\times$ 10^4 counts) relative to the nanorods (Figure 3c, 2.6 $\times$ 10^4 counts) and nanocages (Figure 3d, 2.8 $\times$ 10^4 counts) at 24 h postinjection, which is different from the order observed for biodistribution. Since the Cerenkov luminescence produced from radioactive decay is expected to experience attenuation due to the absorption and scattering by tissues before it reaches the detector, other factors such as intratumoral distribution can have an impact on its intensity. After the animal organs had been harvested, the luminescence signals were mainly detected from liver, spleen, and tumor for all the four types of nanostructures with intensities consistent with the data obtained in biodistribution studies (Figure S4). Previously, we have examined the *in vivo* toxicity of Au nanostructures with a dose of 400 μg/mouse *via* histological analysis and did not observe any toxic effect.[34] In this study, with the administration of Au nanostructures at a less amount, we did not observe any adverse effect either.

Intratumoral Distribution of Nanostructures. In order to better understand the shape dependence of intratumoral distribution for the Au nanostructures, the tumors were excised from the mice at 24 h postinjection, microtomed into multiple slices of about 50 μm thick. The cross sections of these slices were then subjected to autoradiography imaging. Noticeable differences were observed for the Au nanostructures with different shapes. Interestingly, signals associated with the ^{198}Au-incorporated nanostructures were only detected in the periphery of the tumors for both nanospheres (Figure 4a) and nanodisks (Figure 4b), whereas signals were detected throughout the tumor when the mice were injected with either nanorods (Figure 4c) or nanocages (Figure 4d). In addition, for the case of nanorods or nanocages, the strongest signal was located at the core of the tumor. This result offers one explanation for the observation that tumors in the mice injected with the nanospheres or nanodisks showed stronger luminescence than the tumors in mice injected with the nanorods or nanocages. We believe that the Cerenkov radiation was attenuated more significantly when originating from the core rather than the surface of a tumor because the photons had to travel through a thicker layer of tissue before it was detected. Of course, other factors such as the level

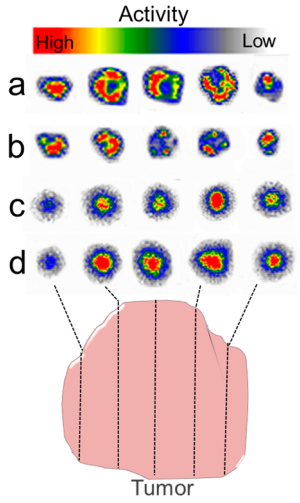

Figure 4. Autoradiographic images of tumor slices at 24 h postinjection of the different types of ^{198}Au-incorporated Au nanostructures: (a) nanospheres, (b) nanodisks, (c) nanorods, and (d) cubic nanocages.

of accumulation also played a role, as supported by the nanospheres, which exhibited both the greatest % ID/g accumulation in tumor and the strongest luminescence intensity in the region of interest (ROI). Moreover, it should be pointed out that the actual size of nanoparticles can also affect the intratumoral distribution profile.[35] A further study comparing the intratumoral distributions of nanoparticles with different sizes will lead to the identification of nanostructure with optimal size and shapes for cancer imaging and therapy.

The accumulation of nanostructures in tumors can be explained by the EPR effect, a well-established phenomenon that plays an important role in both passive and active targeting. This phenomenon, however, only occurs in vascularized tumors, and the efficacy is closely related to the angiogenesis process and tumor vasculature.[14−16,36,37] To validate the involvement of the EPR effect in our system, we used PA imaging to characterize the vasculature in the EMT6 tumor. Figure 5a shows a coronal (top view) maximum amplitude projection (MAP) image, clearly revealing the vasculatures inside the tumor (indicated by the dashed circle) and surrounding tissues. The sagittal (side view) MAP image in Figure 5b shows a well-resolved vasculature to a depth of approximately 2.1 mm. The tumor blood volume quantified by PA imaging was 2.3 ± 0.2 times greater than other tissues, consistent with the fast-growing nature of the EMT6 tumor model.[6] The vasculature present in the EMT6 tumor provides an avenue for the nanostructures to transport into the tumor. The vascularity was further characterized by histological staining (Figure S5) and PET imaging with ^{64}Cu(II) diacetylbis(N^4-methylthiosemicarbazone) (^{64}Cu-ATSM),[38] which was supposed to be localized in the hypoxic regions away from the vasculature. As shown in Figures 6 and S6, the uptake of ^{64}Cu-ATSM was relatively low. Specifically, the tumor was characterized by a standardized uptake value (SUV) of 0.4 ± 0.1, tumor-to-muscle ratio of 2.1 ± 0.4, and accumulation of 2.0 ± 0.6% ID/g for ^{64}Cu-ATSM. The accumulation was much lower than the data (4.2 ± 1.0% ID/g) previously reported for the hypoxic EMT6 tumor at a later stage of development,[39] confirming the well-oxygenated tumor environment and active angiogenesis process during the study period, as shown in Figure 5b.

In general, most solid tumors have a heterogeneous pattern of intratumoral blood vessels. As shown in Figure S5, the vasculature in the EMT6 tumor was largely heterogeneously distributed, with vessel density varying greatly throughout the tumor. We also observed a heterogeneous microenvironment consisting of blood vessels, individual red blood cells associated with the leaky vessels, and necrotic areas containing inflammatory cells. Interestingly, high metabolism in the tumor was confirmed by PET imaging

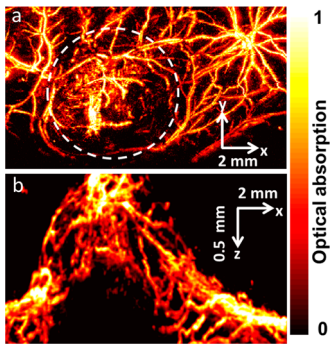

Figure 5. Photoacoustic microscopy images of the EMT6 tumor in a mouse: (a) coronal MAP image viewed from the top and (b) sagittal MAP image viewed from the side.

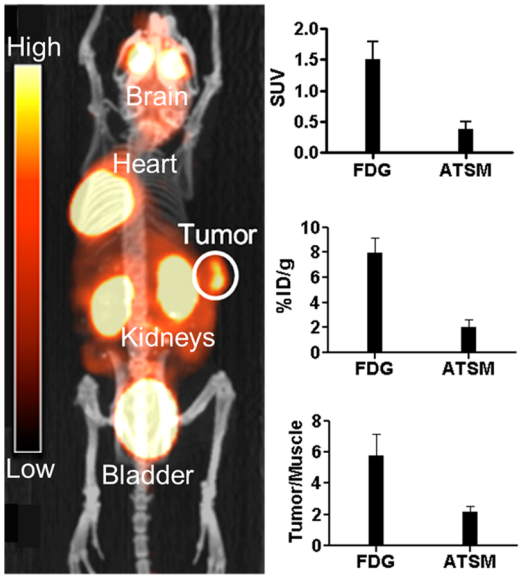

Figure 6. (Left) Co-registered ^{18}F-FDG PET/CT images of a BALB/c mouse bearing a EMT6 tumor. (Right) Quantitative comparisons of standardized uptake values, % ID/g, and tumor/muscle ratios for the ^{18}F-FDG and ^{64}Cu-ATSM tracers.

with ^{18}F-flourinated deoxyglucose (^{18}F-FDG) (Figure 6).[40] Significant tumor uptake of ^{18}F-FDG was observed, with SUV of 1.5 ± 0.3, accumulation of 8.0 ± 1.2% ID/g, and tumor-to-muscle ratio of 5.8 ± 1.4. The ^{18}F-FDG uptake was relatively homogeneous throughout the tumor volume, suggesting a general glycolytic phenotype throughout both aerobic and anaerobic microenvironments, a common characteristic of many types of cancers.

The data from PA imaging, histology staining, and PET imaging all showed the hallmarks expected for the tumor model, including the presence of intratumoral vasculature, heterogeneous microenvironments, and high metabolism of glucose. We can take advantage of these features to deliver nanostructures into tumors for diagnosis and photothermal therapy. While the vasculature serves as an entryway for nanostructures to enter the tumor, it is the convective flow that determines intratumoral distribution of nanostructures.

The nanostructures can accumulate in a tumor by leaking out through the pores in the vascular walls due to the EPR effect. Once outside the vasculature, however, the transport of nanostructures is controlled by diffusion through the hypoxic microenvironments. To be distributed throughout the EMT6 tumor, the nanostructures must be able to flow through the tumor microvasculature, leak out through pores in the vascular walls, and then diffuse through distinct microenvironments containing necrotic, avascular volumes. It has been observed that nanostructures with smaller sizes were able to diffuse deeper into tumors compared to their larger counterparts,[41] and that the transport of nanorods through porous media was mainly determined by the smaller dimension.[27] In this study, all the four colloidal samples of Au nanostructures showed good stability when incubated with 10% fetal bovine serum in phosphate buffer saline at 37 °C for up to 24 h (Figure S7), excluding the possible effect of particle aggregation on the EPR effect. Since the Au nanorods had two of their dimensions less than 15 nm, they should have a better chance to leak out through the small pores in the microvasculature of a tumor and penetrate into the tumor volume, as evidenced by the autoradiography image in Figure 4c. Other factors such as the tumbling motion of a nanorod under flow and the diffusion motion outside the vasculature could also affect its ability to penetrate through the tumor.[42]

The shape of a particle can affect its properties such as the friction coefficient,[42] resistance, and buoyancy.[43] For vasculature-based passive targeting, the convective flow inside the vessels, which also determines the intratumoral distribution of nanoparticles, is largely determined by the pressure difference between the vasculature and the interstitial space of a tumor.[41] Because the nanocage has a hollow core and six flat faces, these factors may significantly increase its convective and diffusive properties in the tumor tissue compared to the spherical counterparts. Additionally, the hollow core gives the nanocage a lower density, which can affect their resistance and increase buoyancy during diffusive transport *in vivo*. As revealed by the autoradiography image in Figure 4d, these effects allow the nanocage to flow through tumor microvasculature, leak out through pores, and diffuse through interstitial tumor space to reach microenvironments inside the entire tumor.

CONCLUSION

In summary, we have demonstrated the synthesis of radioactive Au nanostructures with a similar size but four different shapes by directly incorporating ^{198}Au into their crystal lattices. The radiolabeling integrity and stability associated with these nanostructures have enabled us to quantitatively analyze their biodistribution, tumor uptake, and intratumoral distribution using a murine EMT6 breast cancer model. Specifically, the biodistribution could be quantified by measuring the γ radiation from ^{198}Au, whereas both tumor uptake and intratumoral distribution could be measured by detecting the β^- emission for Cerenkov radiation and autoradiography. Of the four shapes, the ^{198}Au-incorporated nanospheres showed the best blood circulation, the lowest clearance by the reticuloendothelial system, and the highest overall tumor uptake relative to nanodisks, nanorods, and nanocages. Interestingly, nanorods and nanocages could reach the cores of the tumors, whereas nanospheres and nanodisks were only observed on the surfaces of the tumors, suggesting the unique positions of Au nanorods and nanocages for photothermal cancer treatment.[34] Future studies need to focus on further improving the blood circulation half-life and pharmacokinetics of these Au nanostructures to reduce uptake by liver and spleen and minimize radiation burden, test these ^{198}Au nanostructures in other tumor models, and add molecular targeting ligands to their surfaces to increase their tumor uptake for better use of the therapeutic capability provided by the β^- emission and photothermal conversion.

MATERIALS AND METHODS

Chemicals and Reagents. Poly(ethylene glycol)monomethyl ether thiol ($M_w \approx 5000$ Da) was purchased from Laysan Bio (Arab, AL). All other chemicals or reagents, including sodium borohydride ($NaBH_4$), CTAB, chloroauric acid ($HAuCl_4$), ascorbic acid, sodium citrate, silver nitrate ($AgNO_3$), concentrated hydrochloric acid (HCl, 37%), and nitric acid (HNO_3) were obtained from Sigma-Aldrich (St. Louis, MO). All chemicals were used as received.

Preparation of Radioactive $H^{198}AuCl_4$. Proper radiation safety training and personal protection equipment are required because ^{198}Au is a strong β^- emitter (E_{max} = 0.96 MeV, 99% abundance). The ^{198}Au (specific activity = 3.7 GBq/mg) was produced at the University of Missouri using the MURR irradiation facility. Briefly, 5−30 mg of Au foil was irradiated at a flux of 8×10^{13} n/cm^2/s. After irradiation, the radioactive foil was dissolved with 0.4 mL of freshly prepared aqua regia (HCl/HNO_3 = 3/1, v/v) under heating at 90 °C for 5 min. The solution was then dried by heating at 100 °C, reconstituted in 0.4 mL of 0.05 M HCl twice, and finally reconstituted in 0.1 M HCl for shipping. Upon receiving, the sample was dried by heating to 130 °C and reconstituted in ultrapure water. This procedure was repeated three times to remove the acids and nitrogen oxide byproducts. To incorporate ^{198}Au into the lattices of the Au nanostructures, the radioactive $H^{198}AuCl_4$ was mixed with nonradioactive $HAuCl_4$ prior to their use in a synthesis.

Preparation of ^{198}Au-Incorporated Au Nanodisks. The radioactive nanodisks were prepared by etching away the corners of Au triangular nanodisks, which were synthesized by following a previously reported method with the use of 107 MBq of $H^{198}AuCl_4$.[29] After the ^{198}Au-incorporated triangular nanodisks were purified by centrifugation, aqueous $HAuCl_4$ solution (10 mM) in CTAB (100 nM) was added slowly (1−3 μL for each time) into 1 mL of the triangular nanodisks to generate round

nanodisks. The reaction was stopped by centrifugation once the LSPR peak had reached 770 nm.

Preparation of ^{198}Au-Incorporated Au Nanocages. The radioactive nanocages were prepared *via* the galvanic replacement reaction between Ag nanocubes and a mixture of $H^{198}AuCl_4$ and $HAuCl_4$.[31] An aqueous suspension of Ag nanocubes (48 nm in edge length) were prepared, and then titrated with an aqueous solution containing $H^{198}AuCl_4$ (81 MBq) and $HAuCl_4$ (0.75 mM) dropwise (30 mL/h). The reaction was stopped by centrifugation when the LSPR peak had reached 780 nm.

Preparation of ^{198}Au-Incorporated Au Nanospheres. The radioactive nanospheres were prepared *via* seed-mediated growth by using ascorbic acid as a reducing agent and sodium citrate as a colloidal stabilizer.[28] The synthesis involved the use of 59 MBq of $H^{198}AuCl_4$ and 30 nm Au nanospheres as the seeds. The reaction was stopped by centrifugation once the LSPR peak had reached 530 nm.

Preparation of ^{198}Au-Incorporated Au Nanorods. The radioactive nanorods were prepared using a seed-mediated method that involved the addition of a suspension of Au spherical seeds to a growth solution in the presence of CTAB as a capping agent.[30] First, 250 μL of an aqueous $HAuCl_4$ solution (10 mM) was added to 7.5 mL of a 0.1 M CTAB solution in a 20 mL glass vial. Then, 0.6 mL of an aqueous $NaBH_4$ solution (10 mM, ice-cold) was added in one shot under vigorous stirring. The as-obtained nanospheres were used as the seeds for the growth of Au nanorods. In a typical process, 4.75 mL of 0.1 M CTAB, 0.2 mL of 10 mM $HAuCl_4$ containing 7.8 MBq of $H^{198}AuCl_4$, and 30 μL of 10 mM $AgNO_3$ were added stepwise to a glass vial, followed by gentle mixing. The solution at this stage appeared bright brown-yellow in color. Then 32 μL of 0.1 M ascorbic acid was added, and the solution became colorless upon mixing. Finally, 20 μL of the seed solution was added, and the reaction mixture was gently mixed for 10 s and then left undisturbed for 3 h. The specific activities of the four samples of ^{198}Au-incorporated nanostructures are listed in Table S1.

Conjugation of PEG with Au Nanostructures. Four milliliters of the Au nanostructures in ultrapurified H_2O (0.05−0.2 mg/mL in Au content as determined by ICP-MS) was mixed with 2.0 mg of mPEG-SH and incubated overnight at room temperature. The excess mPEG-SH was removed by centrifugation, and the solids were washed three times with ultrapurified H_2O to obtain the PEGylated Au nanostructures.

Electron Microscopy. To determine morphology, the nanoparticles were deposited on TEM grids and examined using a Tecnai G2 Spirit transmission electron microscope (TEM) operated at 120 kV (FEI, Hillsboro, OR).

Tumor Mouse Model. All animal studies were performed in compliance with guidelines set forth by the NIH Office of Laboratory Animal Welfare and approved by the Washington University Animal Studies Committee. The EMT6 murine mammary carcinoma cells (ATCC, Manassas, VA) were cultured in Waymouth's MB 752/1 medium with 85% 2 mM L-glutamine and 15% fetal bovine serum at 37 °C with 5% CO_2. EMT6 cells (2×10^5) in 100 μL saline were injected into the right flank, back, or hind flank of 7 week old female BALB/c mice weighing 15−20 g. Tumors were allowed to grow for 8−10 days, reaching an average size of 100 mm^3, before further studies were performed.

***In Vivo* Biodistribution.** EMT6 tumor-bearing BALB/c mice were anesthetized with inhaled isoflurane before 185−370 kBq of ^{198}Au-incorporated nanospheres (314 kBq, 5.27 μg/mouse), nanodisks (185 kBq, 27.8 μg/mouse), nanorods (326 kBq, 4.22 μg/mouse), or nanocages (225 kBq, 17.9 μg/mouse) (suspended in 100 μL saline) was injected *via* the tail vein. After re-anesthetization, the mice were euthanized by cervical dislocation 1, 6, or 24 h after injection ($n = 4$ animals per time point). Organs of interest were collected, weighed, and counted in a well Beckman 8000 gamma counter (Beckman, Brea, CA). Standards were prepared and measured along with the samples to calculate percentage of the injected dose per gram of tissue (% ID/g).

***In Vivo* Luminescence Imaging.** EMT6 tumor-bearing BALB/c mice ($n = 2$) were anesthetized with isoflurane before 1.79−3.83 MBq of ^{198}Au-incorporated nanospheres (3.83 MBq, 64.7 μg/mouse), nanodisks (2.94 MBq, 442 μg/mouse), nanorods (1.79 MBq, 23.1 μg/mouse), or nanocages (2.48 MBq, 197 μg/mouse) (suspended in 100 μL saline) was injected *via* the tail vein. *In vivo* radioactive optical imaging was performed with an IVIS 100 Spectrum system (PerkinElmer, Waltham, MA). The mouse was placed in a light-tight chamber under isoflurane anesthesia, and luminescent images were acquired over 5 min at 1 and 24 h postinjection. Images were analyzed using Living Image 3.0 software (Caliper Life Sciences, Hopkinton, MA). The optical signal was normalized to p/s/cm^2/sr, and the emission intensity was normalized to the radioactivity injected.

Autoradiographic Imaging. Tumors were excised from the mice after Cerenkov imaging and fixed in 4% paraformaldehyde. The tumors were frozen in Optimal Cutting Temperature compound and then cut with a Vibratome 8850 whole body cryomicrotome (SIMS Co., Ltd., Tokyo, Japan) into 8−20 slices, with each slice being 50 μm thick. The slices were placed on glass slides for 2D autoradiography using an Instant Imager Electronic Autoradiography system (Packard, Meriden, CT). Images were acquired and analyzed with Imager software (Packard, Meriden, CT).

***In Vivo* PA Imaging.** EMT6 tumor-bearing BALB/c mice ($n = 6$) were imaged 8−10 days after injection with EMT6 cells as described above. The PA imaging system was an updated version of what was used in previous publications,[44,45] and it relies on the collection of photoacoustic signals generated from the absorbed laser irradiation. The light source was a tunable dye laser (Cobra, Sirah) pumped by a Nd:YLF laser (INNOSLAB, EdgeWave), providing 7 ns laser pulse width with a pulse repetition rate up to 5 kHz. The output light was coupled into a multimode fiber (M30L02, Thorlabs), passed through a conical lens, and then weakly focused by an optical condenser into the sample. The generated ultrasound signal was collected by the acoustic lens, which was in confocal arrangement with the focused laser beam, and received by a 50 MHz ultrasound transducer (V214-BB-RM, Olympus NDT). For each laser shot, a 1D depth-resolved image (A-line) was acquired without mechanical scanning. By raster-scanning along the transverse plane, a 2D image was acquired, which could be expanded to three dimensions by collecting 2D images at multiple focal planes throughout the tumor volume. Volumetric images can be viewed through either MAP or direct 3D rendering. MAP was performed by projecting the maximum signal amplitude along the z axis (depth) or other axes. A field of view of 12 mm × 10 mm can be acquired within about 1 min. The lateral and axial resolution of the system were 45 and 15 μm, respectively. The pulse energy at the skin surface was about 5 mJ/cm^2, which is well below the standard limit regulated by the American National Standards Institute standards (ANSI Z136.1).

***In Vivo* PET Imaging.** To characterize tumor glucose uptake and hypoxia, PET imaging was performed with ^{18}F-FDG and ^{64}Cu-ATSM, respectively. PET and the corresponding CT images were acquired in either an Inveon microPET/CT scanner (Siemens, Munich, Germany) or a Focus 220 PET scanner (Concorde Microsystems, Knoxville, TN). To measure glucose uptake, EMT6 tumor-bearing BALB/c mice were fasted for 4 h and anesthetized with isoflurane before 11.1 MBq of ^{18}F-FDG acquired from the Washington University cyclotron facility was injected *via* the tail vein. Dynamic scans were acquired every 5 min until 1 h postinjection. Images were analyzed with Inveon software (Siemens, Munich, Germany).

For hypoxia studies, ATSM was first labeled with ^{64}Cu acquired from the Washington University cyclotron facility through a reported protocol.[38] Briefly, 117 MBq of ^{64}Cu was dissolved in 100 μL of water. An aliquot of 5 mL of ATSM reconstitution solution (10% propylene glycol, 1.25% sodium acetate in sterile water) was mixed with 7.5 μg of lyophilized ATSM ligand and vortexed vigorously for 1 min. Then 1 mL of the ATSM stock solution was added to the ^{64}Cu solution and vortexed vigorously for 30 s. Radiochemical purity of the ^{64}Cu-ATSM was tested with an Oasis cartridge (Waters, Milford, MA) and confirmed to be >95% before the sample was diluted with 2 mL saline. EMT6 tumor-bearing BALB/c mice were anesthetized with isoflurane, and 100 μL of saline containing 3 MBq of ^{64}Cu-ATSM was injected *via* the tail vein. Dynamic scans were acquired every 5 min until 1 h postinjection. Images were analyzed with Inveon software (Siemens, Munich, Germany).

Conflict of Interest: The authors declare no competing financial interest.

Acknowledgment. This work was supported by a grant from the NCI (R01 CA138527) and startup funds from Georgia Institute of Technology.

Supporting Information Available: Additional figures and information as described in the text. This material is available free of charge *via* the Internet at http://pubs.acs.org.

REFERENCES AND NOTES

1. Peer, D.; Karp, J. M.; Hong, S.; Farokhzad, O. C.; Margalit, R.; Langer, R. Nanocarriers as an Emerging Platform for Cancer Therapy. *Nat. Nanotechnol.* **2007**, *2*, 751–760.
2. Cobley, C. M.; Chen, J.; Cho, E. C.; Wang, L. V.; Xia, Y. Gold Nanostructures: A Class of Multifunctional Materials for Biomedical Applications. *Chem. Soc. Rev.* **2011**, *40*, 44–56.
3. Huang, X.; Jain, P. K.; El-Sayed, I. H.; El-Sayed, M. A. Gold Nanostructures: Interesting Optical Properties and Recent Applications in Cancer Diagnostics and Therapy. *Nanomedicine* **2007**, *2*, 681–693.
4. Willets, K. A.; Van Duyne, R. P. Localized Surface Plasmon Resonance Spectroscopy and Sensing. *Annu. Rev. Phys. Chem.* **2007**, *58*, 267–297.
5. Mourant, J. R.; Fuselier, T.; Boyer, J.; Johnson, T. M.; Bigio, I. J. Predictions and Measurements of Scattering and Absorption over Broad Wavelength Ranges in Tissue Phantoms. *Appl. Opt.* **1997**, *36*, 949–957.
6. Wang, Y.; Liu, Y.; Luehmann, H.; Xia, X.; Brown, P.; Jarreau, C.; Welch, M.; Xia, Y. Evaluating the Pharmacokinetics and *In Vivo* Cancer Targeting Capability of Au Nanocages by Positron Emission Tomography Imaging. *ACS Nano* **2012**, *6*, 5880–5888.
7. Xu, Y.; Liu, H.; Cheng, Z. Harnessing the Power of Radionuclides for Optical Imaging: Cerenkov Luminescence Imaging. *J. Nucl. Med.* **2011**, *52*, 2009–2018.
8. Lucignani, G. Čerenkov Radioactive Optical Imaging: A Promising New Strategy. *Eur. J. Nucl. Med. Mol. Imaging* **2011**, *38*, 592–595.
9. Thorek, D. L. J.; Robertson, R.; Bacchus, W. A.; Hahn, J.; Rothberg, J.; Beattie, B. J.; Grimm, J. Cerenkov Imaging: A New Modality for Molecular Imaging. *Am. J. Nucl. Med. Mol. Imaging* **2012**, *2*, 163–173.
10. Chanda, N.; Kan, P.; Watkinson, L. D.; Shukla, R.; Zambre, A.; Carmack, T. L.; Engelbrecht, H.; Lever, J. R.; Katti, K.; Fent, G. M.; *et al.* Radioactive Au Nanostructures in Cancer Therapy: Therapeutic Efficacy Studies of GA-198AuNP Nanoconstruct in Prostate Tumor-Bearing Mice. *Nanomed. Nanotechnol.* **2010**, *6*, 201–209.
11. Wang, Y.; Liu, Y.; Luehmann, H.; Xia, X.; Wan, D.; Cutler, C.; Xia, Y. Radioluminescent Au Nanocages with Controlled Radioactivity for Real-Time *In Vivo* Imaging. *Nano Lett.* **2013**, *13*, 581–585.
12. Gatenby, R. A.; Gillies, R. J. A Microenvironmental Model of Carcinogenesis. *Nat. Rev. Cancer* **2008**, *8*, 56–61.
13. Matsumura, Y.; Maeda, H. A New Concept for Macromolecular Therapeutics in Cancer Chemotherapy: Mechanism of Tumoritropic Accumulation of Proteins and the Antitumor Agent Smancs. *Cancer Res.* **1986**, *46*, 6387–6392.
14. Jain, R. K.; Stylianopoulos, T. Delivering Nanomedicine to Solid Tumors. *Nat. Rev. Clin. Oncol.* **2009**, *7*, 653–664.
15. Hashizume, H.; Baluk, P.; Morikawa, S.; McLean, J. W.; Thurston, G.; Roberge, S.; Jain, R. K.; McDonald, D. M. Openings between Defective Endothelial Cells Explain Tumor Vessel Leakiness. *Am. J. Pathol.* **2000**, *156*, 1363–1380.
16. Sarin, H.; Kanevsky, A. S.; Wu, H.; Sousa, A. A.; Wilson, C. M.; Aronova, M. A.; Griffiths, G. L.; Leapman, R. D.; Vo, H. Q. Physiologic Upper Limit of Pore Size in the Blood-Tumor Barrier of Malignant Solid Tumors. *J. Transl. Med.* **2009**, *7*, 51.
17. Ernsting, M. J.; Murakami, M.; Roy, A.; Li, S. Factors Controlling the Pharmacokinetics, Biodistribution and Intratumoral Penetration of Nanoparticles. *J. Controlled Release* **2013**, *172*, 782–794.
18. Smith, B. R.; Cheng, Z.; De, A.; Koh, A. L.; Sinclair, R.; Gambhir, S. S. Real-Time Intravital Imaging of RGD-Quantum Dot Binding to Luminal Endothelium in Mouse Tumor Neovasculature. *Nano Lett.* **2008**, *8*, 2599–2606.
19. Kong, G.; Braun, R. D.; Dewhirst, M. W. Hyperthermia Enables Tumor-Specific Nanoparticle Delivery: Effect of Particle Size. *Cancer Res.* **2000**, *60*, 4440–4445.
20. Doshi, N.; Prabhakarpandian, B.; Rea-Ramsey, A.; Pant, K.; Sundaram, S.; Mitragotri, S. Flow and Adhesion of Drug Carriers in Blood Vessels Depend on Their Shape: A Study Using Model Synthetic Microvascular Networks. *J. Controlled Release* **2010**, *146*, 196–200.
21. Tan, J.; Shah, S.; Thomas, A.; Ou-Yang, H. D.; Liu, Y. The Influence of Size, Shape and Vessel Geometry on Nanoparticle Distribution. *Microfluid. Nanofluid.* **2013**, *14*, 77–87.
22. Kersey, F.; Merkel, T. J.; Perry, J.; Napier, M. E.; DeSimone, J. M. The Effect of Aspect Ratio and Deformability on Nanoparticle Extravasation through Nanopores. *Langmuir* **2012**, *28*, 8773–8781.
23. Venkataraman, S.; Hedrick, J. L.; Ong, Z. Y.; Yang, C.; Ee, P. L. R.; Hammond, P. T.; Yang, Y. Y. The Effects of Polymeric Nanostructure Shape on Drug Delivery. *Adv. Drug Delivery Rev.* **2011**, *63*, 1228–1246.
24. Doshi, N.; Mitragotri, S. Macrophages Recognize Size and Shape of Their Targets. *PLoS One* **2010**, *5*, e10051.
25. Zhang, K.; Fang, H.; Chen, Z.; Taylor, J. S. A.; Wooley, K. L. Shape Effects of Nanostructures Cnjugated with Cell-Penetrating Peptides (HIV Tat PTD) on CHO Cell Uptake. *Bioconjugate Chem.* **2008**, *19*, 1880–1887.
26. Smith, B. R.; Kempen, P.; Bouley, D.; Xu, A.; Liu, Z.; Melosh, N.; Dai, H.; Sinclair, R.; Gambhir, S. S. Shape Matters: Intravital Microscopy Reveals Surprising Geometrical Dependence for Nanostructures in Tumor Models of Extravasation. *Nano Lett.* **2012**, *12*, 3369–3377.
27. Chauhan, V. P.; Popovic, Z.; Chen, O.; Cui, J.; Fukumura, D.; Bawendi, M. G.; Jain, R. K. Fluorescent Nanorods and Nanospheres for Real-Time *In Vivo* Probing of Nanoparticle Shape-Dependent Tumor Penetration. *Angew. Chem., Int. Ed.* **2011**, *123*, 11619–11622.
28. Ziegler, C.; Eychmüller, A. Seeded Growth Synthesis of Uniform Au Nanoparticles with Diameters of 15−300 nm. *J. Phys. Chem. C* **2011**, *115*, 4502–4506.
29. Millstone, J. E.; Wei, W.; Jones, M. R.; Yoo, H.; Mirkin, C. A. Iodide Ions Control Seed-Mediated Growth of Anisotropic Au Nanostructures. *Nano Lett.* **2008**, *8*, 2526–2529.
30. Huang, X. H.; El-Sayed, I. H.; Qian, W.; El-Sayed, M. A. Cancer Cell Imaging and Photothermal Therapy in the Near-Infrared Region by Using Gold Nanorods. *J. Am. Chem. Soc.* **2006**, *128*, 2115–2120.
31. Skrabalak, S. E.; Au, L.; Li, X.; Xia, Y. Facile Synthesis of Ag Nanocubes and Au Nanocages. *Nat. Protoc.* **2007**, *2*, 2182–2190.
32. Zhang, G.; Yang, Z.; Lu, W.; Zhang, R.; Huang, Q.; Tian, M.; Li, L.; Liang, D.; Li, C. Influence of Anchoring Ligands and Particle Size on the Colloidal Stability and *In Vivo* Biodistribution of Polyethylene Glycol-Coated Gold Nanoparticles in Tumor-Xenografted Mice. *Biomaterials* **2009**, *30*, 1928–1936.
33. LipKa, J.; Semmler-Behnke, M.; Sperling, R. A.; Wenk, A.; Takenaka, S.; Schleh, C.; Kissel, T.; Parak, W. J.; Kreyling, W. G. Biodistribution of PEG-Modified Gold Nanoparticles Following Intratracheal Instillation and Intravenous Injection. *Biomaterials* **2010**, *31*, 6574–6581.
34. Wang, Y.; Black, K. C. L.; Luehmann, H.; Li, W.; Zhang, Y.; Cai, X.; Wan, D.; Liu, S. Y.; Li, M.; Kim, P.; *et al.* Comparison Study of Au Nanohexapods, Nanorods, and Nanocages for Photothermal Cancer Treatment. *ACS Nano* **2013**, *7*, 2068–2077.
35. Lee, H.; Fonge, H.; Hoang, B.; Reilly, R. M.; Allen, C. The Effects of Particle Size and Molecular Targeting on the Intratumoral and Subcellular Distribution of Polymeric Nanoparticles. *Mol. Pharmaceutics* **2010**, *7*, 1195–1208.
36. McDonald, D. M.; Baluk, P. Significance of Blood Vessel Leakiness in Cancer. *Cancer Res.* **2002**, *62*, 5381–5385.
37. Fukumura, D.; Jain, R. K. Tumor Microvasculature and Microenvironment: Targets for Anti-angiogenesis and Normalization. *Microvasc. Res.* **2007**, *74*, 72–84.

38. Lewis, J. S.; Laforest, R.; Dehdashti, F.; Grigsby, P. W.; Welch, M. J.; Siegel, B. A. An Imaging Comparison of ^{64}Cu-ATSM and ^{60}Cu-ATSM in Cancer of the Uterine Cervix. *J. Nucl. Med.* **2008**, *49*, 1177–1182.
39. Lewis, J. S.; McCarthy, D. W.; McCarthy, T. J.; Fujibayashi, Y.; Welch, M. J. Evaluation of Cu-64-ATSM *in Vitro* and *in Vivo* in a Hypoxic Tumor Model. *J. Nucl. Med.* **1999**, *40*, 177–183.
40. Champion, L.; Lerebours, F.; Cherel, P.; Edeline, V.; Giraudet, A. L.; Wartski, M.; Bellet, D.; Alberini, J. L. ^{18}F-FDG PET/CT Imaging *versus* Dynamic Contrast-Enhanced CT for Staging and Prognosis of Inflammatory Breast Cancer. *Eur. J. Nucl. Med. Mol. Imaging* **2013**, *40*, 1206–1213.
41. Chauhan, V. P.; Stylianopoulos, T.; Martin, J. D.; Popović, Z.; Chen, O.; Kamoun, W. S.; Bawendi, M. G.; Fukumura, D.; Jain, R. K. Normalization of Tumour Blood Vessels Improves the Delivery of Nanomedicines in a Size-Dependent Manner. *Nat. Nanotechnol.* **2012**, *7*, 383–388.
42. Shah, S.; Liu, Y.; Hu, W.; Gao, J. Modeling Particle Shape-Dependent Dynamics in Nanomedicine. *J. Nanosci. Nanotechnol.* **2011**, *11*, 919–928.
43. Teeguarden, J. G.; Hinderliter, P. M.; Orr, G.; Thrall, B. D.; Pounds, J. G. Particokinetics *in Vitro*: Dosimetry Considerations for *In Vitro* Nanoparticle Toxicity Assessments. *Toxicol. Sci.* **2007**, *95*, 300–312.
44. Zhang, H. F.; Maslov, K.; Stoica, G.; Wang, L. V. Functional Photoacoustic Microscopy for High-Resolution and Noninvasive *In Vivo* Imaging. *Nat. Biotechnol.* **2006**, *24*, 848–851.
45. Stein, E. W.; Maslov, K.; Wang, L. V. Noninvasive, *In Vivo* Imaging of the Mouse Brain Using Photoacoustic Microscopy. *J. Appl. Phys.* **2009**, *105*, 102027.